The Astrophysical Journal, 956:85 (17pp), 2023 October 20 https://doi.org/10.3847/1538-4357/acf4f1

High-resolution Observations of the Low Atmospheric Response to Small Coronal Heating Events in an Active Region Core

Paola Testa[1], Helle Bakke[2,3], Luc Rouppe van der Voort[2,3], and Bart De Pontieu[2,3,4]
[1] Harvard-Smithsonian Center for Astrophysics, 60 Garden St, Cambridge, MA 02193, USA; ptesta@cfa.harvard.edu
[2] Rosseland Centre for Solar Physics, University of Oslo, P.O. Box 1029 Blindern, N-0315 Oslo, Norway
[3] Institute of Theoretical Astrophysics, University of Oslo, P.O. Box 1029 Blindern, N-0315 Oslo, Norway
[4] Lockheed Martin Solar & Astrophysics Laboratory, 3251 Hanover St, Palo Alto, CA 94304, USA
Received 2023 June 23; revised 2023 August 22; accepted 2023 August 28; published 2023 October 11

Abstract

High-resolution spectral observations of the lower solar atmosphere (chromosphere and transition region) during coronal heating events, in combination with predictions from models of impulsively heated loops, provide powerful diagnostics of the properties of the heating in active region cores. Here, we analyze the first coordinated observations of such events with the Interface Region Imaging Spectrograph (IRIS) and the CHROMospheric Imaging Spectrometer (CHROMIS), at the Swedish 1 m Solar Telescope (SST), which provided extremely high spatial resolution and revealed chromospheric brightenings with spatial dimensions down to ∼150 km. We use machine-learning methods (*k*-means clustering) and find significant coherence in the spatial and temporal properties of the chromospheric spectra, suggesting, in turn, coherence in the spatial and temporal distribution of the coronal heating. The comparison of IRIS and CHROMIS spectra with simulations suggests that both nonthermal electrons with low energy (low-energy cutoff ∼5 keV) and direct heating in the corona transported by thermal conduction contribute to the heating of the low atmosphere. This is consistent with growing evidence that nonthermal electrons are not uncommon in small heating events (nanoflare to microflares), and that their properties can be constrained by chromospheric and transition region spectral observations.

Unified Astronomy Thesaurus concepts: Solar physics (1476); Active sun (18); Active solar corona (1988); Solar active regions (1974); Solar atmosphere (1477); Solar chromosphere (1479); Solar chromospheric heating (1987); Solar coronal heating (1989); Solar coronal loops (1485); Solar ultraviolet emission (1533); Solar transition region (1532); Solar extreme ultraviolet emission (1493)

1. Introduction

The understanding of the physical processes converting magnetic energy into thermal energy and powering the solar outer atmosphere represents one of the main open issues in solar physics (e.g., Klimchuk 2006; Reale 2014; Testa & Reale 2023). The heating is generally predicted to be impulsive (e.g., Klimchuk 2015), and on small spatial scales (below the current resolution capabilities). Direct observational diagnostics of coronal heating are therefore often difficult to obtain.

Tracers of coronal heating can sometimes be more evident in observations of the lower solar atmosphere—transition region (TR) and chromosphere—which efficiently radiates energy excesses, rather than in the highly conductive corona, where the signatures of heating release are easily washed out. Furthermore, while the coronal emission in a pixel is due to contributions from a generally complex three-dimensional system of loops, the TR is relatively unencumbered by contamination of other material along the line of sight. It is therefore easier to detect and study single heating events in the TR, and derive constraints on the coronal event properties. For these reasons, the moss (the bright TR of high pressure loops; e.g., Peres et al. 1994; Berger et al. 1999; Fletcher & De Pontieu 1999) is well suited to investigate the properties of coronal heating in the core of ARs (e.g., Martens et al. 2000; Antiochos et al. 2003; Testa et al. 2013, 2014, 2020).

The temporal variability of the moss has been studied in imaging and spectral observations, and its relatively constant emission has often been attributed to steady heating of active region (AR) cores (e.g., Antiochos et al. 2003; Brooks et al. 2009; Tripathi et al. 2010). However, the high spatial (∼0.″3) and temporal resolution EUV imaging data, with the High-resolution Coronal Imager (Kobayashi et al. 2014) sounding rocket, have provided evidence of TR brightenings on short timescales (down to ∼15 s) at the footpoints of transient hot loops (Testa et al. 2013). Follow-up TR spectral observations at high spatial, temporal, and spectral resolution with the Interface Region Imaging Spectrograph (IRIS; De Pontieu et al. 2014), together with 1D hydrodynamic RADYN models of nanoflare-heated loops—including nonlocal thermodynamic equilibrium (non-LTE), and heating by beams of nonthermal electrons (NTE) as well as in situ thermal heating— provided powerful diagnostics of the properties of coronal heating and mechanisms of energy transport (Testa et al. 2014, 2020; Cho et al. 2023). Polito et al. (2018), Testa et al. (2020) discussed the IRIS diagnostics of the coronal heating properties from spectral observations of moss brightenings. Bakke et al. (2022) recently extended those investigations to ground-based observations, deriving additional diagnostics of the heating properties from lower chromospheric emission.

In this paper, we analyzed coordinated chromospheric AR observations, with the Swedish 1 m Solar Telescope (SST; Scharmer et al. 2003a, 2003b), and with IRIS, as well as coronal observations with the Solar Dynamics Observatory (SDO)/the Atmospheric Imaging Assembly (AIA), for a small heating event in an AR. The very high resolution chromospheric observations

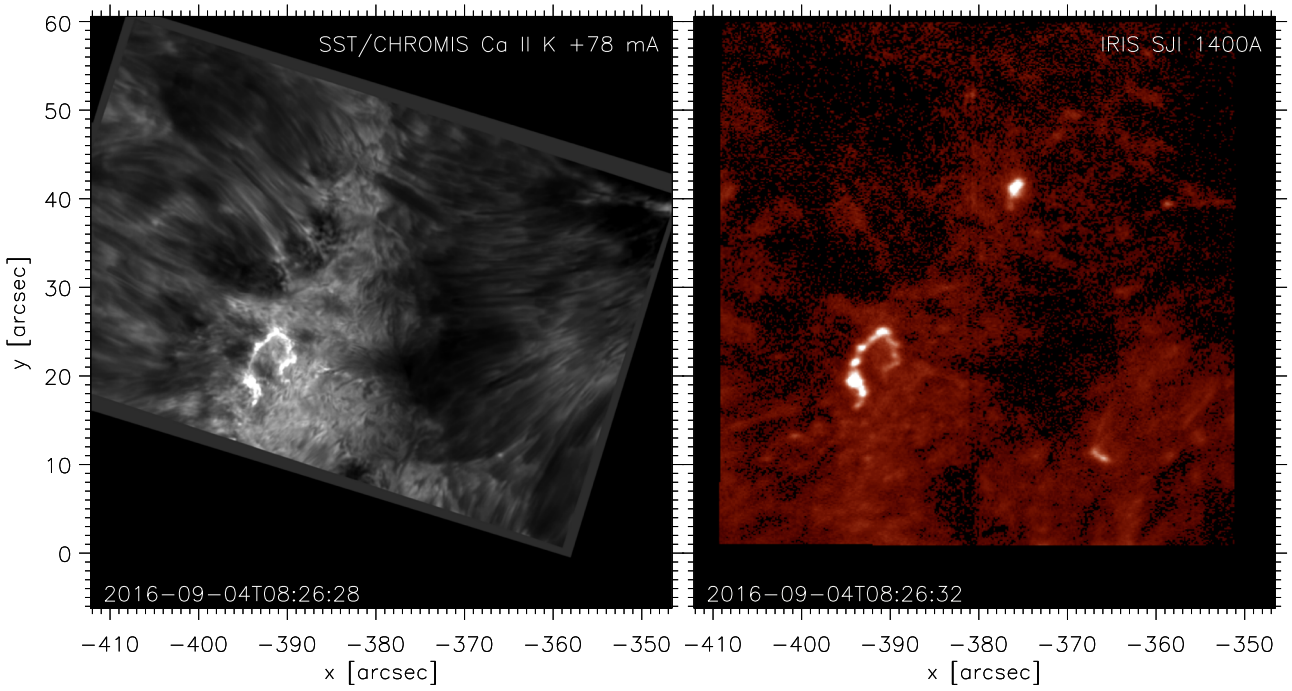

Figure 1. Chromospheric and TR observations in AR 12585 with SST/CHROMIS and IRIS on 2016 September 04 around 08:26UT. Left: SST/CHROMIS image at the center wavelength of Ca II (at 3934 Å). Right: IRIS slit-jaw image (SJI) in the 1400 Å band. The bright S-shaped region corresponds to brightenings at the footpoints of hot loops undergoing short-lived heating, as illustrated in the context coronal images presented in Figure 2.

spectra from SST provide new constraints to the models of small heating events. A *k*-means analysis of these SST spectra allows us to detect coherence in the spatial and temporal distribution of the chromospheric emission, and, in turn, to speculate on the coherence of the spatial and temporal distribution of the heating properties. IRIS spectral observations provide insights into the chromospheric and TR properties. In Section 2, we describe the selected data, and their analysis and comparison with expectations from numerical simulations is presented in Section 3. In Section 4, we summarize and discuss our findings, and draw our conclusions.

2. Observations and Data Analysis

The detection of small (nanoflare to microflare) coronal heating events in coordinated IRIS and SST observations of active regions is one of the goals of the multiyear campaign we have conducted since the IRIS launch in 2013 (Rouppe van der Voort et al. 2020). In fact, SST and IRIS provide very useful complementary high-resolution observations of the photosphere and chromosphere that can greatly enhance the scientific impact of either separate instrument.

Here, we focus on one of the first such events observed during the SST and IRIS coordinated campaign. In particular, we selected the observations of AR 12585 carried out on 2016 September 4 (Figures 1 and 2 show images of this event observed by SST, IRIS, and SDO). This data set is part of the database of publicly available SST and IRIS coaligned data sets described in Rouppe van der Voort et al. (2020), and some analysis of it has been presented by Rouppe van der Voort et al. (2017).

The SST telescope includes dual Fabry–Pérot filtergraph systems capable of fast wavelength sampling of spectral lines: the CRisp Imaging SpectroPolarimeter (CRISP; Scharmer et al. 2008), and the CHROMospheric Imaging Spectrometer (CHROMIS; Scharmer 2017), with field of view (f.o.v.) of approximately $1' \times 1'$. CRISP has a plate scale of $0.''058$ per pixel, and the SST diffraction limit is $0.''14$ at the wavelength of the Hα line (calculated as λ/D with $\lambda = 6563$Å, and D=0.97 m as the diameter of the SST aperture). The CHROMIS instrument (installed in 2016) has a plate scale of $0.''038$ per pixel, and the diffraction limit is $0.''08$ at the wavelength of the Ca II K line (∼3933.7 Å). The data we analyze here were acquired during the first CHROMIS campaign (Rouppe van der Voort et al. 2017; Vissers et al. 2019). Here, we mainly focus on the analysis of the chromospheric Ca II K data. The Ca II K line was sampled at 21 wavelength positions, between $\pm$ 100 km s^{-1} Doppler offset from line center. The line was sampled with 6 km s^{-1} steps (or 78 mÅ) between $\pm$ 54 km s^{-1} and somewhat coarser in the rest of the wavelength range. In addition, a continuum position was sampled at 4000 Å. The CRISP instrument was running a program sampling the H α line at 15 line positions between $\pm$ 68 km s^{-1}, and Ca II8542 Å at 21 line positions between $\pm$61 km s^{-1}. The data were processed following the CRISPRED reduction pipeline (de la Cruz Rodríguez et al. 2015) and an early version of the CHROMISRED pipeline (now both are incorporated into SSTRED, Löfdahl et al. 2021). Seeing-induced deformations were corrected for using Multi-Object Multi-Frame Blind Deconvolution (van Noort et al. 2005) image restoration. The CHROMIS time series has a cadence of ∼22 s; the CRISP time series has a cadence of 20 s. The wavelength calibration of the SST/CHROMIS observations has been performed by using an average profile over a quiet area just prior to the observations, and deriving the wavelength within the Ca IIline where the intensity is at a minimum value. This reference wavelength is given the value (3933.6841 Å) of the wavelength of the Ca II K line minimum in the Fourier Transform Spectrometer atlas (Neckel 1999).

We note that particularly the CHROMIS observations have exceptionally high spatial resolution (∼100 km), which can

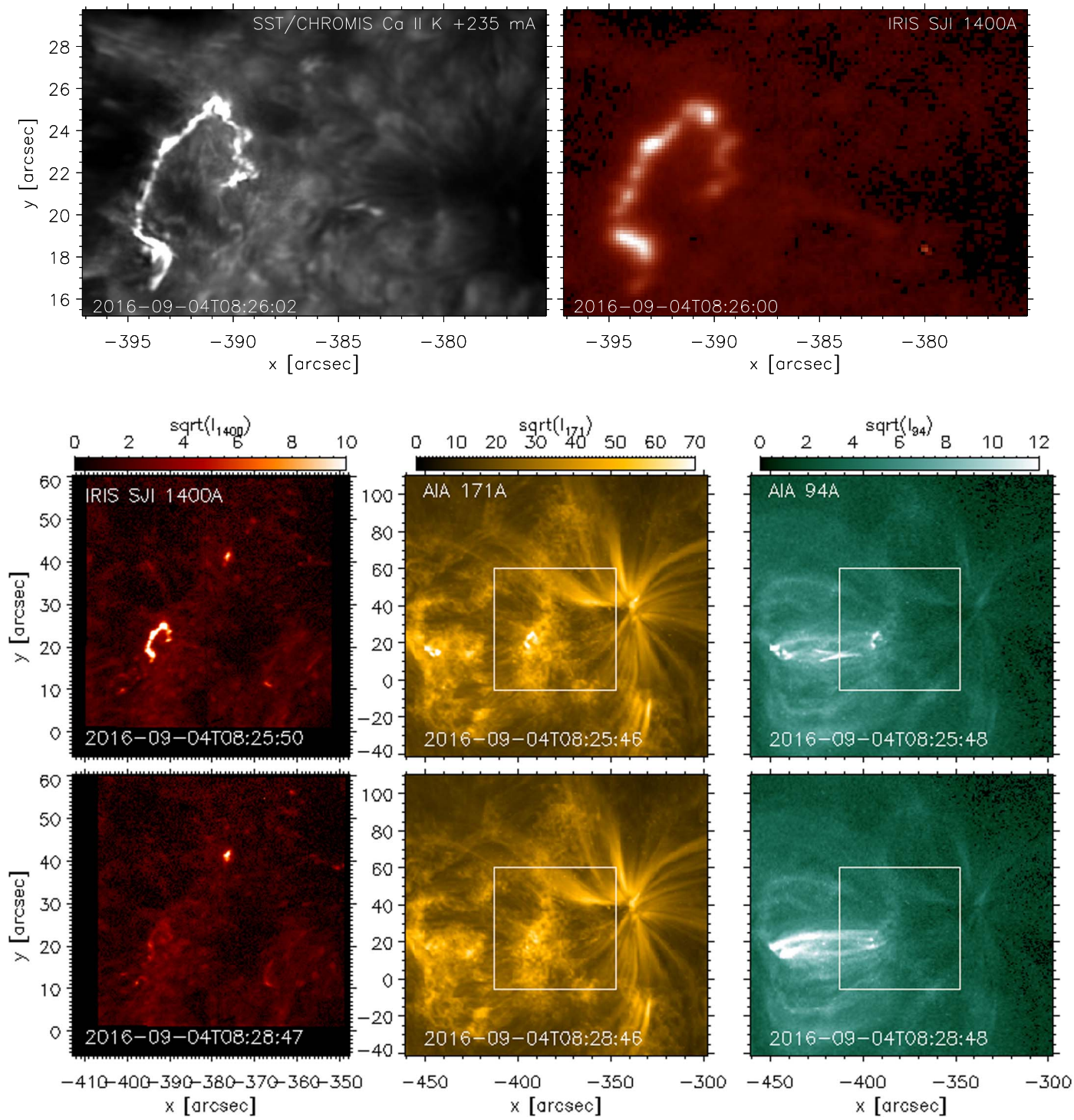

Figure 2. SST, IRIS, and SDO coordinated observations of AR 12585. In the top panels, we plot zoomed in versions of the images of Figure 1 showing emission in the Ca II K core (left) and IRIS 1400 Å SJI (right). The bottom panels show the TR and coronal emission, for two times—one at the peak of the loop footpoint chromospheric emission (top), and one 3 minutes later (bottom) when the overlying hot coronal loops are bright. In particular, we show, from left to right: the TR emission in the IRIS SJI 1400 Å passband; the upper TR emission in the AIA 171 Å narrow band, dominated by ∼1 MK emission from Fe IX; the coronal emission in the AIA 94 Å narrow band (which has a cooler, ∼1 MK, component, and a hot $\gtrsim$4 MK component). For the AIA emission, we show a larger f.o.v. than that from the corresponding IRIS observations. We mark with white boxes the f.o.v. of the IRIS SJI.

constrain significantly better the spatial distribution of the heating events.

IRIS observes chromospheric and TR emission in UV at high spatial and temporal resolution with both high-resolution spectroscopy and slit-jaw imaging (SJI). The IRIS observations we analyze here are medium dense 16 step rasters (OBSID 3625503135), with an exposure time of 0.5 s, and raster steps of 0.″35, covering a f.o.v. of about 5″×60″ (in about 21 s). The slit-jaw images were recorded in the SJI 1400 Å (dominated by Si IV lines), 1330 Å (dominated by C II lines), and 2796 Å (Mg II k core) channels at a temporal cadence of about 10 s. We use IRIS calibrated level 2 data, which have been processed for dark

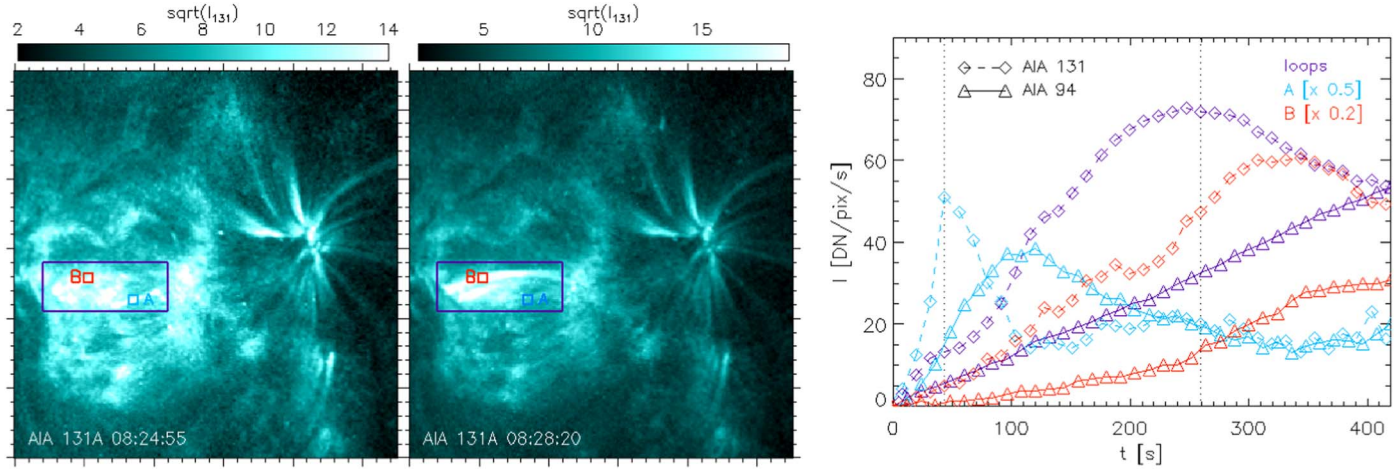

Figure 3. Evolution of the hot coronal emission in the AR core during the heating event. The left two panels show the coronal emission in the SDO/AIA 131 Å passband (the 131 Å emission in the transient core loops is dominated by hot Fe XXI emission), and for the same f.o.v. of the other AIA passbands shown in Figure 2, at two times (close to the beginning of the heating event and a few minutes later). Three locations are marked in these images to identify interesting coronal features: a short hot loop brightening early in the event (*A*), a location in a longer loop at the footpoints of which the chromospheric and TR brightenings are observed as shown in Figure 1 and 2 (*B*), and a larger region (purple rectangle) including most of the dynamic hot loops anchored in the ribbon shown in the previous two figures. The right panel shows lightcurves ($t = 0$ corresponds to 2016-09-04T08:24:00) in the hot AIA passbands at 131 Å (diamonds), and 94 Å (triangles), for the three regions marked in the left panels. For the *A* and *B* locations, the intensities are averaged over 5×5 pixel regions (i.e., $\sim 3'' \times 3''$). All lightcurves are subtracted of their minimum value in the considered temporal window. The vertical dotted lines mark the times of the two images shown in the left panels.

current, flat field, and geometrical corrections (De Pontieu et al. 2014). The SST and IRIS observations were aligned through cross-correlation of image pairs in the Ca II K wing and SJI 2796 Å (see Rouppe van der Voort et al. 2020, for more details). The alignment between Ca II K and SJI 2796 Å appears to be accurate down to the IRIS SJI pixel size (0.″166). The short exposure time of the IRIS program (0.5 s) resulted in a high noise level in the SJI images, in particular in SJI 1400 Å and SJI 1330 Å. The fiducial marks that are added to the IRIS spectrograph slit are difficult to identify in individual SJI images and even impossible to identify in SJI 1400 Å. This makes the alignment between the SJI channels challenging as the fiducial marks are the basis for accurate cross alignment. To improve on the SJI alignment as part of the standard IRIS level 2 data processing, we summed over many SJI exposures to reduce the noise level and improve the visibility of the fiducial marks. It is clear that this procedure improved the alignment, but it cannot be excluded that there remains a residual misalignment on the order of 1 or 2 pixels between SJI 2796 Å and SJI 1400 Å.

We also use coordinated imaging observations of a coronal emission, taken with AIA (Lemen et al. 2012) on board SDO (Pesnell et al. 2012). The AIA data sets are characterized by 0.″6 pixels, and 12 s cadence, and observe the TR and corona across a broad temperature range (Boerner et al. 2012, 2014). We used the AIA data cubes coordinated with and coaligned to the IRIS data sets, which are distributed from the IRIS search data page.[5] These AIA time series appear to be affected by unusual and significant (i.e., several AIA pixels) instabilities in the spatial pointing. We therefore refined the coalignment, by using a cross-correlation routine (tr_get_disp). We use AIA coronal data to investigate the spatial and temporal properties of the coronal emission.

3. Results

AR 12585 appeared at the east limb around 2016 August 30, and it was characterized by sustained coronal activity around Geostationary Operational Environmental Satellites[6] (GOES) B level. An inspection of the time series of the hot emission in the SDO/AIA channels (especially the 94 Å and the 131 Å channels, which include emission from Fe XVIII and Fe XXI lines respectively) shows hot ($\gtrsim$5 MK) dynamic loops in the AR core, although the X-ray emission in the GOES X-ray passbands did not exceed C level for most of the disk passage (from September 1 onward).

The observations we analyze here captured one of these heating events associated with hot coronal emission. In Figure 2, we show the chromospheric, TR, and coronal emission in the AR at two times of this event: early on, when the energy is most likely impulsively released and the chromospheric and TR emission at the loops' footpoints is bright; and a few minutes later, when the coronal plasma in the overlying loops is sufficiently hot and dense to emit brightly in the AIA 94 Å passband.

In the initial impulsive phase of the heating, the chromosphere and TR present rapid and intense brightenings at the footpoints of the heated loops, similar to flare ribbons, as observed by SST and IRIS and shown in Figures 1 and 2 where almost simultaneous images of the chromospheric and TR emission are presented.

3.1. Coronal Properties and Evolution

The heating event appears to involve many coronal structures, including the longer ($\sim$40 Mm in length) coronal structures overlying the bright ribbons we focus on, as well as shorter ($\sim$20 Mm in length) loops overlying a ribbon brightening about a minute earlier (see center row of Figure 2, and Figure 3). In Figure 3, we show the lightcurves for the hot emission observed by AIA in the 94 Å and 131 Å channels. The lightcurves are obtained by subtracting the background value in the same spatial location just before the event, to highlight the evolution of the hot emission. The observed hot

[5] https://iris.lmsal.com/search/

[6] https://www.swpc.noaa.gov/products/goes-x-ray-flux, https://www.ngdc.noaa.gov/stp/satellite/goes/index.html

emission shows the typical behavior observed in other microflares (see, e.g., Testa & Reale 2020), with a rapid increase in the Fe XXI emission (131 Å) in the early phases of the event followed by a cooling phase in which the 131 Å emission decreases while the cooler Fe XVIII 94 Å emission increases. An approximate temperature diagnostic from the 131 Å/94 Å ratio (see, e.g., Testa & Reale 2020) suggests peak coronal temperatures around 8–10 MK, analogous to what is typically found in similar transient events in AR cores (e.g., Reale et al. 2019a; Testa & Reale 2020; Testa et al. 2020).

3.2. Morphology of the Ribbon

The comparison of the two SST and IRIS emission maps shown in Figures 1 and 2 clearly illustrates the differences in morphology in different atmospheric layers, as well as (particularly in Figure 2) the extremely high spatial resolution attained in this SST data set by the CHROMIS instrument. Figure 4 shows measurements of the cross-sectional widths of the ribbon brightenings. There are small spatial offsets of about 0.″2 between corresponding brightenings in Ca II K and SJI 1400 Å. Given the differences in formation heights and the geometry of the observed coronal loops, spatial offsets could be expected, and they might provide valuable information on the 3D morphology of the loop system. We can expect a small offset between the different diagnostics due to differences in formation height, but we are cautious about drawing firm conclusions since we cannot exclude that the offset might be due to a large extent to errors in the alignment between the different passbands. Furthermore, the ribbons evolve very fast, and the SST and IRIS diagnostics are not recorded strictly simultaneously, so some of the apparent offsets could be attributed to temporal evolution.

We measured the cross-sectional widths as full width half maxima for which the half maxima were determined from the difference between the peak intensity and the highest intensity of the two neighboring minima. For these six representative examples, the widths in Ca II K vary between 0.″22 and 0.″36. The widths in SJI 1400 Å are more than 2 times larger and vary between 0.″51 and 0.″84. We note that the narrowest width of 0.″51 corresponds to three IRIS pixels. In feature (D), the cross-sectional profile of the Ca II K image has two narrow peaks while the corresponding feature in SJI 1400 Å is much wider and fuzzier and does not show substructure. The profiles (A)–(F) are shown for red wing Ca II K at +235 mÅ (+18 km s^{-1}), which is the Doppler offset of the peak for most of the redshifted ribbon profiles. The widths of cross-sectional profiles from Ca II K images summed over the full observed spectral widths are only slightly wider. We note how, closer to the two ends of the ribbon (i.e., S of $y \sim 45$, or W of $x \sim -390$, such as, e.g., location (C) at the N-W end), the relative intensity of the CHROMIS Ca II emission with respect to the IRIS SJI 1400 Å emission is much larger than for most other locations, whereas in other locations such as, e.g., E, the TR emission is significantly enhanced with respect to the lower chromospheric emission. As we will discuss more later (see Section 4), these ratios provide clues to the heating properties and transport mechanisms (e.g., harder NTE will likely cause stronger enhancements in the deeper atmosphere, i.e., lower chromosphere, than in the TR).

3.3. k-means Analysis of SST Chromospheric Spectra

To investigate the spatial and temporal evolution of the spectral properties of the chromospheric brightenings, we applied *k*-means clustering analysis (e.g., Panos et al. 2018; Bose et al. 2019) to the SST/CHROMIS Ca II K spectral data. The *k*-means clustering algorithm finds spectral profiles representative of the observed spectra, and it groups the observed spectra according to their spectral properties. The grouping of the large number of observed spectra in a limited number of clusters, each characterized by a representative spectral profile (RSP), allows us to model more easily the variety of observed profiles, and, in turn, to efficiently derive the spatial distribution and temporal evolution of the coronal heating properties. We used the *k*-means clustering algorithm (MacQueen 1967), which partitions data into k predefined clusters that each have a cluster center, which is the average of the data points within that cluster. The clusters are then improved through an iterative process where data points are assigned to a cluster such that the Euclidean distance between the points and the cluster center is minimal. For every iteration, new cluster centers are calculated from the clusters in the previous iteration until the cluster centers do not change, and convergence is reached. A limitation to this method is that the resulting clusters depend significantly on the initial selection of clusters centers. An option is to select the cluster centers at random, but then the initial cluster centers can be close to each other, and more iterations are needed in order to reach convergence. We used the *k*-means++ initialization method (Arthur & Vassilvitskii 2007), which, before defining new cluster centers, draws the cluster centers randomly from the data set such that they are as far away as possible from the previous centers.

In order to determine the optimal number of clusters, we used the elbow technique (see, e.g., Panos et al. 2018 for a discussion), and we found that 60 clusters are sufficient to characterize the selected subset of SST/CHROMIS spectral observations. The 60 RSPs we obtained from this *k*-means analysis are plotted in Figure 5. In Figure 6, we show the spatial distribution of the RSPs in the region of the ribbon, and the corresponding RSPs, which show that the Ca II K line observed in the ribbon varies from blueshifted, and generally narrower, profiles to redshifted, and typically broader, profiles. While the observed blueshifts are generally mild ($\lesssim$10 km s^{-1}), some redshifts reach large values (up to $\sim$25 km s^{-1}). The largest blueshifts are mostly observed in the southern portion of the ribbon. The spatial distribution of the RSPs shows a spatial coherence of the observed spectral profiles, with spatial clusters of several sizes from a few pixels ($\gtrsim$0.″1) to $\sim$50 pixels ($\sim$2″), in one spatial dimension.

We investigated how the spatial distribution of the Ca II K spectral profiles is evolving during the event, as shown in Figure 7, where we plot the maps of RSP distribution for six consecutive time steps of the CHROMIS observations covering most of the ribbon evolution. These plots show that the spatial coherence of the spectral profiles is observed for all time steps, and they reveal several additional interesting features. The highest Doppler shifts are not present in the initial Ca II K profiles (time step (17)), but they appear in the second time step when higher intensities are observed in the ribbon. In fact, the highest Ca II K intensity regions are generally characterized by large and broad redshifted profiles (RSPs (7) and (14), red and orange respectively). Blueshifted profiles are observed only in

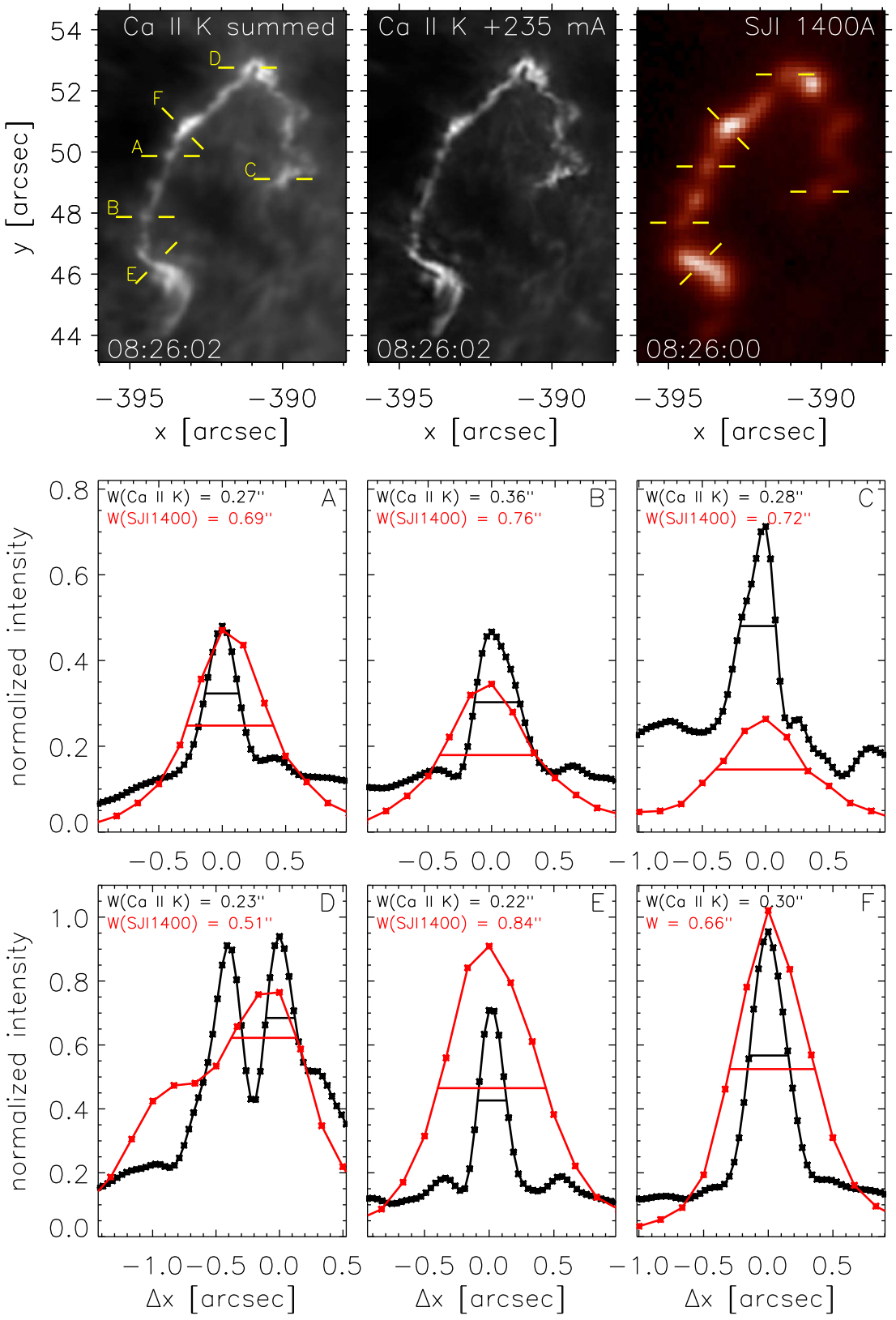

Figure 4. Cross-sectional widths of brightenings in the flare ribbon from CHROMIS and IRIS observations. The top left panel shows an image integrated over the full observed width of the Ca II K line ($\pm$100 km s^{-1}); the top middle panel shows a Ca II K red wing image at around the peak of most redshifted flare profiles. The top right panel shows the corresponding IRIS SJI 1400 Å image. All images are scaled linearly between their respective minima and maxima. The yellow lines mark the endpoints of the the paths (A)–(F) along which intensity profiles were extracted and are shown in the bottom panels. In the bottom panels, the black line is the intensity profile measured in Ca II K + 0.235 Å; the red line in SJI 1400 Å. The full width half maxima are marked with horizontal lines, and their values are given in each panel.

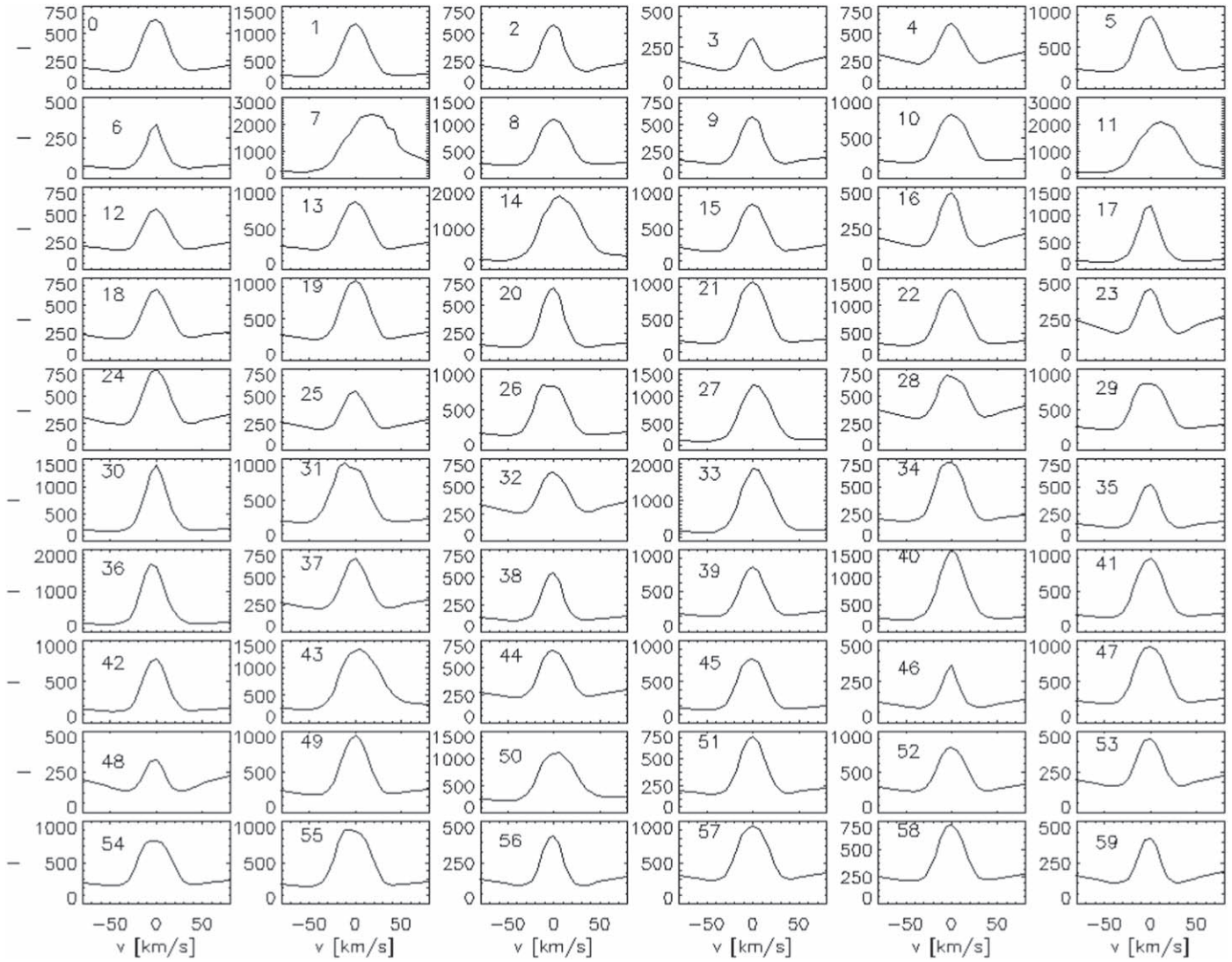

Figure 5. Representative spectral profiles (RSP) obtained from *k*-means analysis, using 60 clusters (see text for a discussion), of the time series of SST/CHROMIS Ca II K spectra.

lower-intensity regions of the ribbon, and only in the southern portion of the ribbon. In this southern region of the ribbon (around coordinates [160, 170] in time step (18); see Figure 6), there is a patch of broad blueshifted profiles (RSP (31) of Figures 5 and 6), where the spectra rapidly shift to broad redshifted profiles in the next time step (19) when the Ca II K intensities in that region increase significantly. We note that for similar events observed with IRIS (e.g., Testa et al. 2014, 2020; Cho et al. 2023) the observed chromospheric and TR spectral profiles significantly change on short timescales of seconds. In light of this, the relatively modest cadence of these CHROMIS data might not provide us with a comprehensive view of the spectral evolution at the loops footpoints. The temporal evolution of the Ca II K spectra in the spatial locations where the highest intensities are observed appear to generally follow a progression from broad profiles with largest redshifts at the peak intensity to progressively less redshifted profiles (i.e., red to orange, to yellow, to green, in terms of the RSPs shown in Figure 5). Figure 7 shows that, as the event progresses, the ribbon, especially the southern portion, advances mostly in the north direction. As new locations in the lower atmosphere get brighter, they tend to be characterized initially by blueshifted and narrow Ca II K profiles, and then evolve to brighter, broader, and more redshifted profiles. This observed evolution of the spectral profiles could be due to the change in the plasma conditions in a magnetic strand, where increasing density and temperature as a consequence of the heating cause a different response to the heating properties, and/or could point to different heating properties during the events, with harder nonthermal electron distributions in newly reconnected lines evolving in time to softer distributions.

In the above *k*-means clustering analysis applied to the SST f.o.v., which includes both ribbon and nonribbon emission, only a few clusters describe the ribbon spectra (see Figure 6). Therefore, in order to refine our analysis of the specific spectral features of the flare profiles, we run a *k*-means analysis on a subset mostly comprised of spectral profiles from the flare ribbon. We used a reduced data set that covers 550 pixels in x and 500 pixels in y centered on the flare ribbon, including the 82 time steps. To find the profiles covering the flare, we sampled all profiles with maximum intensity above 1565 in arbitrary intensity units (see contours in Figure 10). This value was found by exploring different thresholds and see how adjusting it affected the clustering of flare profiles. We also

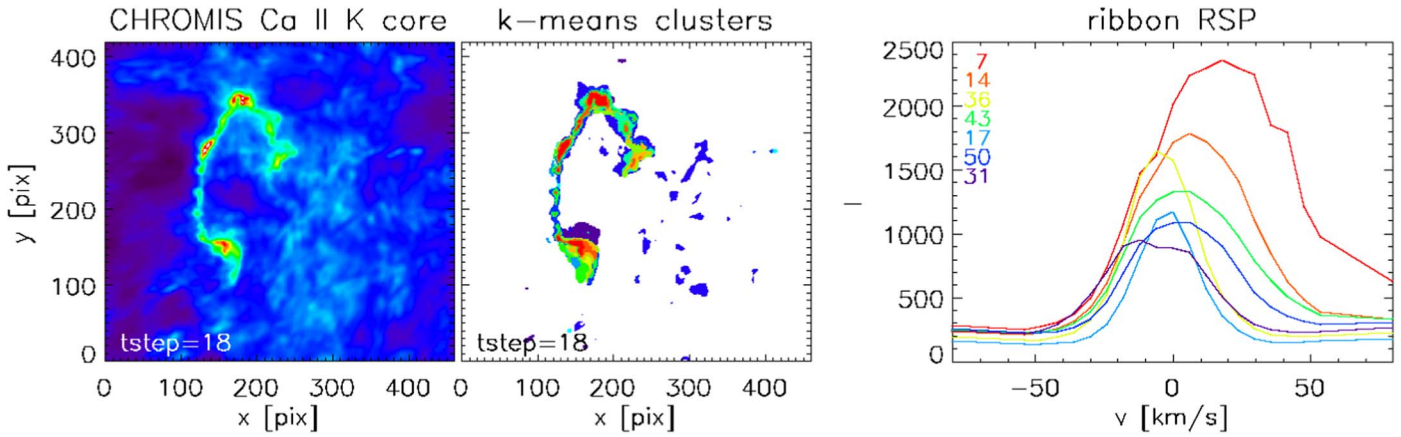

Figure 6. Example of machine-learning analysis of SST/CHROMIS chromospheric spectral observations of variability at the footpoints of hot loops. We show results of *k*-means clustering analysis applied to a subset of the SST/CHROMIS Ca II K spectral data. We selected the f.o.v. shown here and 14 time steps covering the heating event shown in Figure 1, and a few time steps prior to it. The *k*-means clustering algorithm finds spectral profiles representative of the observed spectra, and it groups the observed spectra according to their spectral properties (in this example, we find 60 clusters are sufficient to group the observed spectra). Here, we show, for one time step during the brightenings (the intensity in the Ca II K line core is shown in the left panel), the spatial distribution (middle panel) of the few clusters occurring in the footpoint regions, and the corresponding representative spectral profiles (RSP; right panel; the *k*-means analysis is run on the whole time series, and it produces a single set of RSPs). The RSPs present a variety of properties including broad blueshifted (cluster (31); purple) and redshifted profiles (e.g., clusters (7), (14), (43), (50)).

included profiles from outside the ribbon, creating a total sample of 94,823 profiles, where 62% are flare profiles, and 38% are profiles sampled in the surroundings but outside the flare. We set the number of clusters to 36 in order to capture more details of the profiles, as well as to make sure that specific features end up in less populated clusters. The *k*-means algorithm was applied to the training data set, and the output was used to predict the closest RSPs for each profile in this reduced data set.

Figure 8 shows an overview of the 36 clusters. We applied a Gaussian fit to the RSPs in order to calculate their Doppler shifts and used these values to order the clusters according to their Doppler shift. The number of redshifted RSPs is significantly higher than that of the blueshifted RSPs. In addition, the Doppler shifts to the red generally have higher values. Because of this, we set two different thresholds on the RSPs characterized by redshifts and blueshifts: +5 and $-1\,\mathrm{km\,s^{-1}}$, respectively (see red and blue dashed lines in Figure 9). Following these thresholds, Figure 8 shows that RSPs (1)–(5) are shifted to the blue, RSPs (6)–(14) have weak to no Doppler shifts, and RSPs (15)–(32) are shifted to the red. RSPs (33)–(36) are large clusters containing the profiles from outside the ribbon, and their respective RSPs have $0\,\mathrm{km\,s^{-1}}$ Doppler shift. We note that the profiles in the latter clusters are only used as a reference and are not included in the rest of the analysis; hence, the corresponding RSPs are placed at the end of the sorting. The figure shows that the *k*-means clustering is able to identify and properly cluster specific features. This is seen from the density distributions, showing that the majority of profiles in each cluster are centered around or close to the RSPs.

Figure 9 shows two scatter plots between the Doppler shift and RSP line core widths (left) and the Doppler shift and maximum intensity of the RSPs (right). The color of the ellipses follows the respective Doppler shift of the RSPs. The vertical radii of the ellipses in the left panel are proportional to the maximum intensity of the RSPs, while the horizontal radii of the ellipses in the right panel are proportional to the width of the RSP line cores. The left panel shows that there is a correlation between the Doppler shift and the line core width, where larger Doppler shifts mostly result in broadening of the line cores. This is also clearly seen from the horizontal radii of the ellipses in the right panel. This panel also shows that the maximum intensity of the RSPs is not strongly correlated to the Doppler shift.

The Doppler shift of the flare profiles is further explored in Figure 10, showing intensity maps of the SST/CHROMIS Ca II K line core at six consecutive time steps during the flare. While the top panels of each time step are overplotted with contours marking the threshold for the *k*-means training sampling, the bottom panels show the Doppler shift of every profile in RSPs (1)–(32). The results are similar to those found in Figure 7, where blueshifted profiles are exclusively found in low-intensity areas in the lower part of the ribbon and are not present until $t = 19$. The most redshifted profiles (RSPs (31) and (32)) only occur at $t = 18$ in the top part of the ribbon. Even though the profiles in these clusters exhibit the strongest redshifts, they are generally not the most intense profiles found in the flare. While there indeed are a few profiles in these clusters with high intensity (see density distribution in Figure 8), RSP (21) contains profiles with significantly higher intensities but much lower Doppler shifts (approximately $+9\,\mathrm{km\,s^{-1}}$). This cluster is also a clear outlier in the right panel in Figure 9. We generally see that the regions with high Ca II K intensity are characterized by redshifted profiles, but we note that there are still lower-intensity regions with profiles that are significantly redshifted and broadened (for example RSPs (23), (25), (27), and (29)) as well as high-intensity regions with profiles that are less redshifted and not as broad (for example RSPs (8), (17), (19), and (21)).

3.4. IRIS and SST Spectra

IRIS can provide additional chromospheric and TR diagnostics. Although the brightest portion of the ribbon-like region is unfortunately not under the IRIS slit, the slit crosses a weaker portion of the ribbon, where we can analyze the IRIS and CHROMIS spectral profiles. In Figure 11, we highlight this

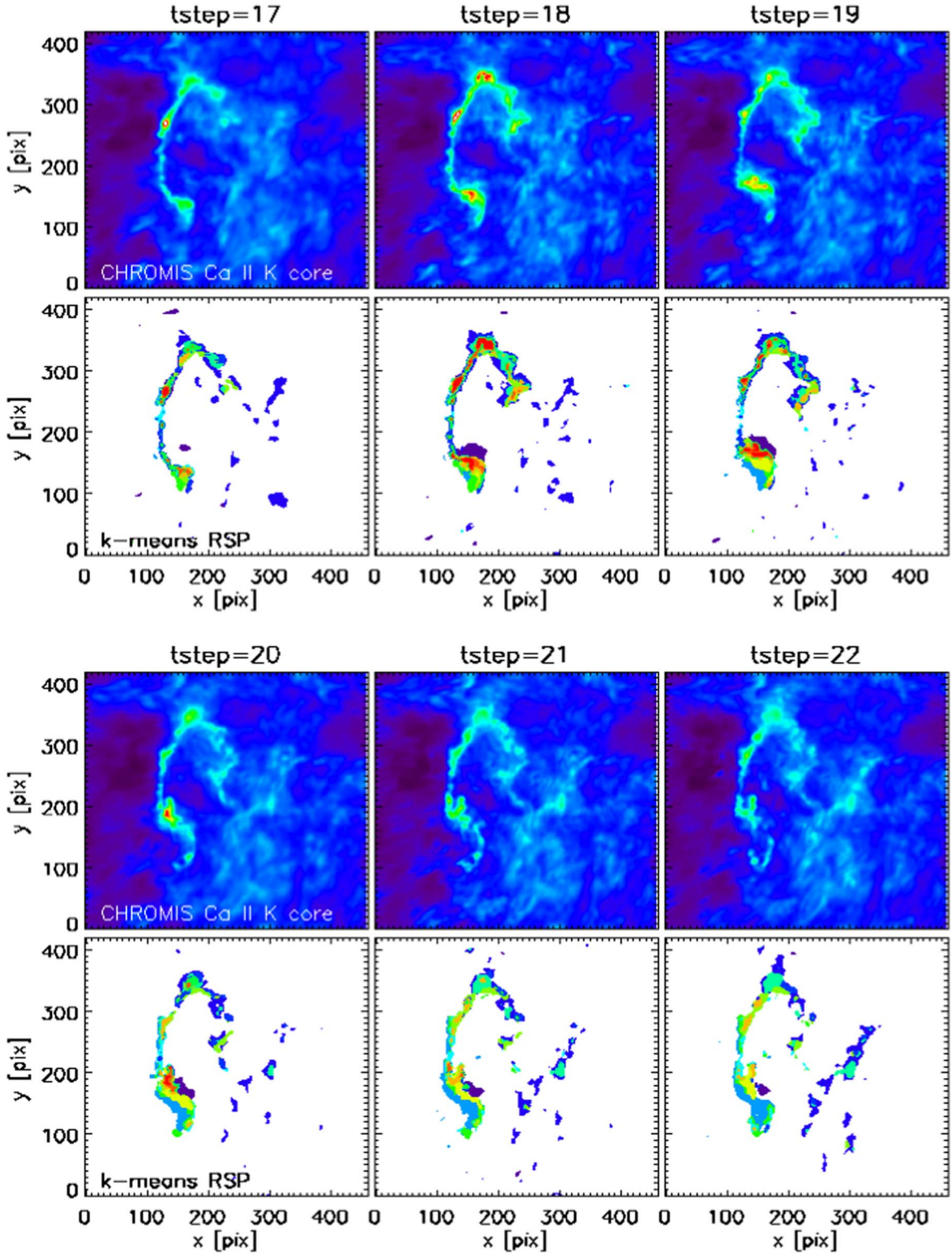

Figure 7. Results of the *k*-means clustering analysis allow to investigate the spatial and temporal evolution of the spectral properties of the chromospheric brightenings. Here, we show, for six consecutive time steps (about 22 s apart) during the brightenings (the intensity in the Ca II K line core is shown in the top panels for each time step), the spatial distribution (bottom panels for each time step) of the few clusters occurring in the footpoint regions, corresponding to the representative spectral profiles shown in Figure 6 (right panel).

weak ribbon region by showing the base difference and running difference IRIS SJI time series: for the base difference, we subtract the initial emission (we chose 2016-09-04T08:19:35 as reference time), whereas for the running difference we subtract the image of the immediately preceding time step. These figures show the presence of a *tail* of the ribbon extending from (x,y) $\approx$ ($-387''$, $22''$) to (x,y) $\approx$ ($-382''$, $18''$), where the latter is in the IRIS spectrograph f.o.v. Another location under the IRIS slit, around (x,y) $\sim$ ($-382''$, $17''$), is also undergoing short-lived brightenings a couple of minutes earlier, and

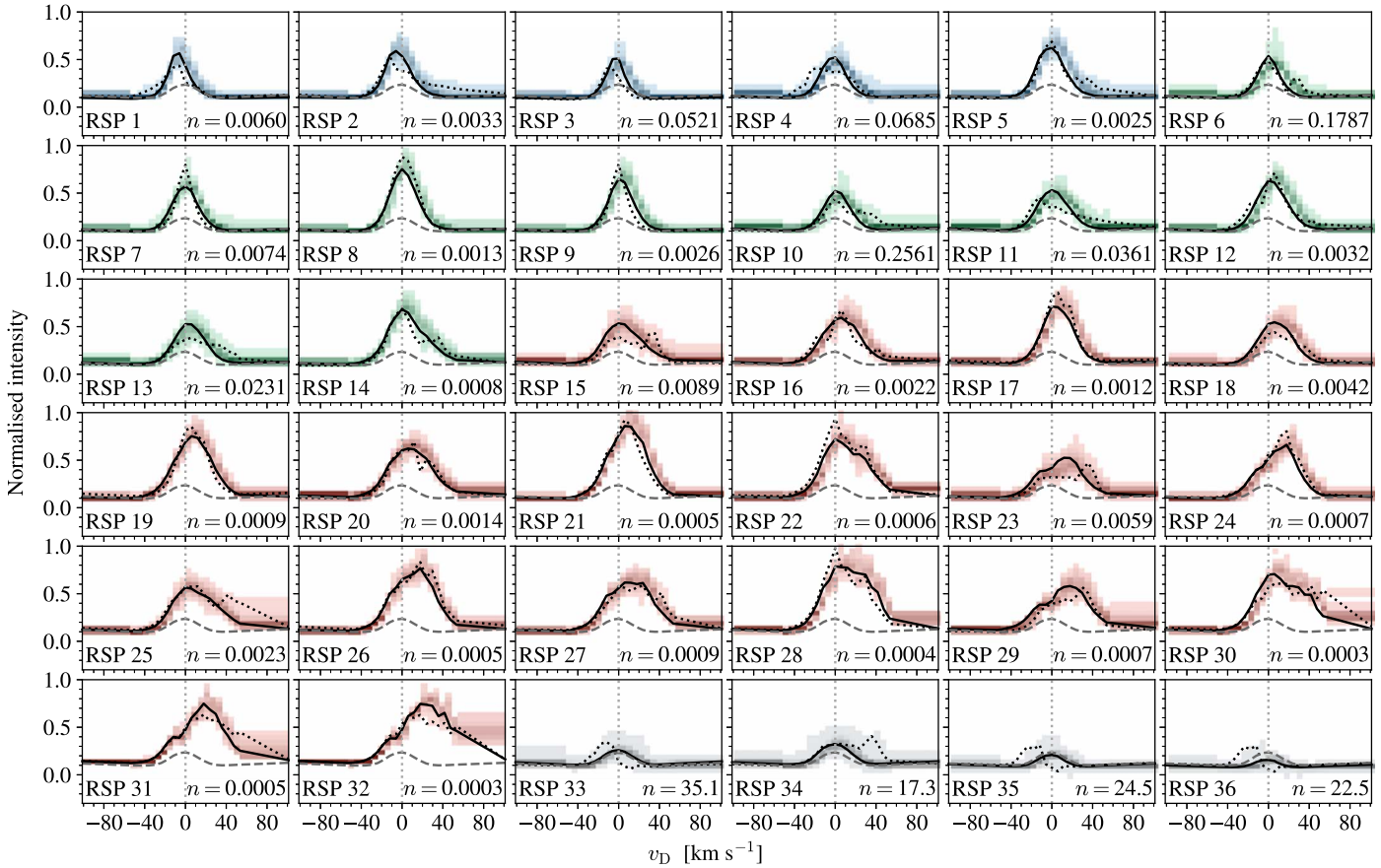

Figure 8. Thirty-six RSPs from the *k*-means clustering of the Ca II K line profiles from a reduced data set focused on the ribbon (see also Figure 10). Each panel shows the RSPs (solid black), the average profile in the reduced data (dashed gray), and the Ca II K profile that have the largest Euclidean distance to the RSP (dotted black). All profiles have been normalized from the lowest to the highest intensity of the reduced data set. The panels include the density distribution of all profiles within a cluster, where darker color indicates higher density. The color of the density distributions in RSPs (1)–(32) also represent the Doppler shift of the RSPs to indicate blueshifts (blue), redshifts (red), and weak to no shifts (green). RSPs (33)–(36) are clusters of profiles outside the flare ribbon, and the gray shading is the density distribution of all profiles in the clusters. RSPs (1)–(32) are sorted by the Doppler shift of the Gaussian profiles that were fitted to the RSPs, and RSPs (33)–(36) are placed at the end of the sorting. *n* represents the number of profiles in a cluster as a percentage of the total amount of profiles in the reduced data set ($\sim 2.25 \times 10^7$ profiles).

appears to be associated with the early brightening of the shorter coronal loops (see left panel of Figure 3). In Figure 12, we show the time series of the spectral profiles in some of the strongest IRIS TR and chromospheric lines, and in the CHROMIS Ca II K, for these two locations (note that we average the IRIS spectra over 3 IRIS pixels along the *y*-axis to improve the signal-to-noise). The earlier brightening (bottom row of Figure 12, and southernmost square marked in Figure 11) shows (1) a significant increase in the Si IV TR emission lasting about a minute and characterized by a blueshift of $\sim$20 km s^{-1} (relative to the pre-event spectrum), and a broad (multipeaked) profile with a small red tail; (2) a very modest increase in C II emission; (3) a modest increase in chromospheric Mg II emission, which is mostly characterized by limited central reversal, and a blue peak slightly more pronounced than the red peak; (4) the CHROMIS Ca II K profiles are similar to the profiles observed in the regions of the main ribbon with weaker emission, i.e., they are single peaked, narrow, and with modest Doppler shift (e.g., RSPs (17), (36) of Figures 5 and 6, or RSPs (7)–(13) of Figures 8 and 9). The second brightening, in the weak *tail* of the ribbon (top row of Figure 12, and northernmost square marked in Figure 11), is slightly longer lasting (about a couple of minutes), and it shows (1) Si IV emission without significant Doppler shift with respect to the pre-event profile (but redshifted in absolute terms); (2) C II emission with relative increase, with respect to the pre-event profile, comparable to the Si IV emission; (3) the chromospheric Mg II and Ca II emission are similar to the other brightening, with largely single-peaked profiles and CHROMIS Ca II K profiles similar to the weaker ribbon regions. For both brightenings, there is no significant Mg II triplet emission detected. In the following subsection (Section 3.5), we will compare the observed profiles with predictions from 1D RADYN models of impulsively heated loops.

3.5. Comparison with Numerical Simulations

Numerical simulations can provide a great deal of insight when interpreting observations. In previous work (Polito et al. 2018; Testa et al. 2020; Bakke et al. 2022), we used 1D flare simulations to investigate the atmospheric response to heating by nanoflares. Several models were carried out using the RADYN numerical code (Carlsson & Stein 1992, 1995, 1997; Allred et al. 2015), which models plasma magnetically confined in a 1D loop structure, by solving the equation of charge conservation and the level population rate equations. RADYN also solves non-LTE radiation transport for H, He, and Ca II, which is necessary when modeling chromospheric

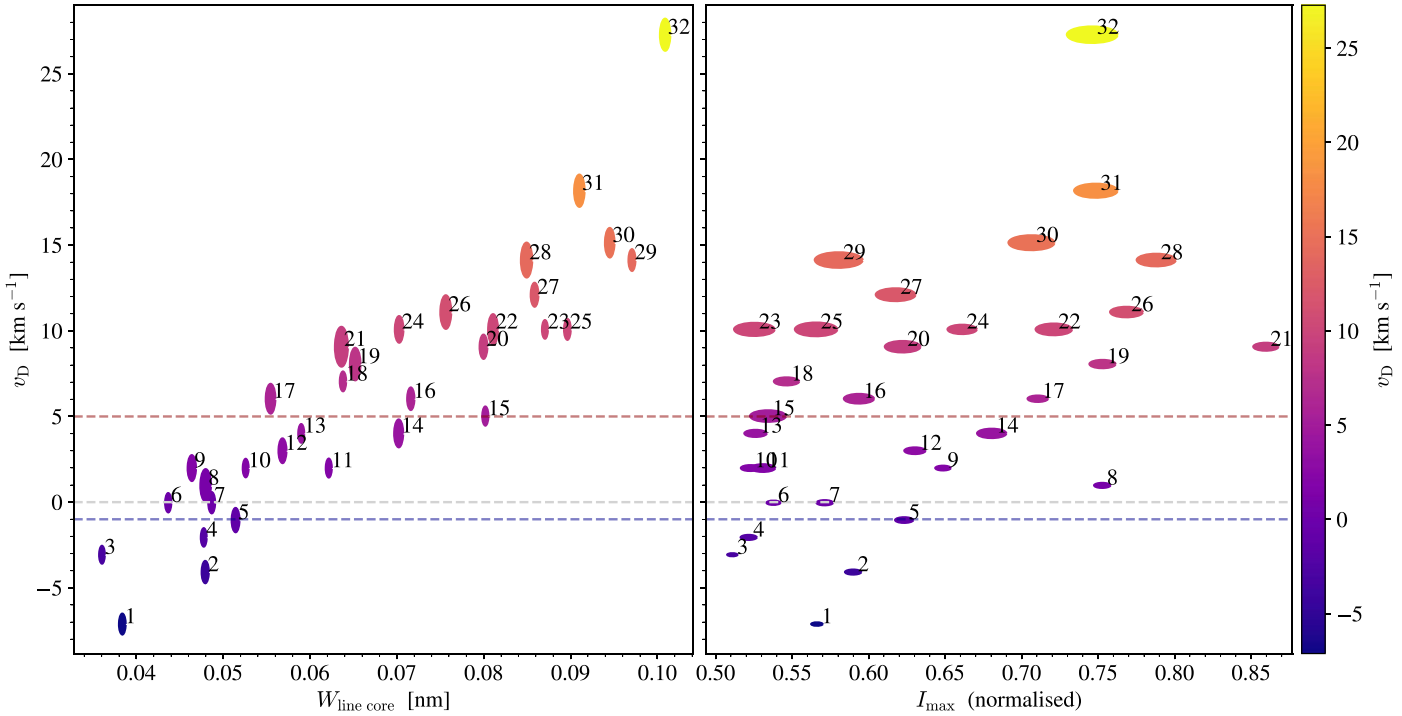

Figure 9. Scatter plots between the Doppler shift and RSP line core widths (left), and Doppler shift and maximum intensity of the RSPs (right). The points are marked with their respective RSP index (see Figure 8), and colored based on their Doppler shift. The vertical radii of the ellipses in the left figure reflect the magnitude of the maximum intensity of the RSPs, while the horizontal radii in the right figure represent the RSP line core widths. The red dashed line at $+5$ km s^{-1} and blue dashed line at -1 km s^{-1} indicate the boundaries for the RSP sorting.

emission. The RADYN version described in Allred et al. (2015) includes the effect of NTE, using the Fokker–Planck equations, and the electron energy distribution is assumed to follow a power law. Details on the RADYN numerical code and the simulations of nanoflare-heated loops are discussed in Polito et al. (2018). In the following, we provide a brief description of the models.

The RADYN simulations of nanoflare-heated loops investigate a broad parameter space including different nanoflare energies, loop-top temperatures, and half-loop lengths. The simulations also include different heating models, such as thermal conduction, electron beam heating with varying low-energy cutoff values E_C, as well as hybrid models of both thermal conduction and electron beams. In Bakke et al. (2022), we focused our efforts on selected models with transport by NTE, where the chromospheric lines were synthesized using the RH 1.5D radiative transfer code (Uitenbroek 2001; Pereira & Uitenbroek 2015). By comparing the Ca II K, Hα, and Ca II 8542 Å synthetic spectra from these models to the flare profiles from the observations, we find that the RADYN model most capable of reproducing the observed spectra is the model with 15 Mm half-loop length and initial loop-top temperature of 1 MK. This particular model has a low-energy cutoff value $E_C = 5$ keV (representing an electron beam with low-energy electrons in the distribution), a spectral index $\delta = 7$ for the power-law energy distribution, and total energy $E = 6 \cdot 10^{24}$ erg deposited in the loop. Figure 13 shows the time evolution of Ca II K, Hα, and Ca II 8542 Å from the RADYN simulation and at three different locations in the flare ribbon, where the latter is given in the top row panels. The locations were chosen in order to show the time evolution of the profiles in a region of strong redshifts (panel (a)), a region of high intensity (panel (b)), and a region of blueshifts (panel (c)). We note that there is a discrepancy between the flare timescales of the RADYN simulation and the observation. In the RADYN model, the flare lasts for 10 s, while in the observation the flare lasts for minutes. The RADYN model was originally meant to simulate short-lived (10–30 s) footpoint brightenings in TR moss as observed with IRIS (Testa et al. 2013, 2014, 2020; Cho et al. 2023). Even though the observed flare is a sequence of many short-lived brightenings, it becomes difficult to make a temporal comparison between the profiles because the time between each observed frame is about half the total simulation time. The comparisons made in this work are therefore focused on the shape and features of the profiles rather than the timescales.

The shape of the RADYN Ca II K and Ca II 8542 Å profiles does not resemble that of the observations, especially since the absorption feature of the synthetic spectral lines is not seen in the observed flare profiles. However, the strong redshift of the Ca II K profile is consistent with the observation at the peak of the flare (around 6.8 min) at the the locations marked in panels (a) and (b) of Figure 13. The largest Doppler shift of the Ca II K line observed in the northern part of the ribbon (panel (a)) is comparable to that of the RADYN simulation, where the lines from both the observation and simulation have components that are redshifted to a value between 30 and 35 km s^{-1}.

Hα is the synthetic profile from RADYN that is most similar to the observational profiles. In particular, the Hα profile from the location marked in panel (b) has an almost identical shape to the one from RADYN, although with a slightly smaller range of velocity on the red side of the line profile. The evolution of the profiles is also similar, where the initial profiles are in absorption until the flare phase during which both profiles are in emission and characterized by a redshifted component with multiple peaks. In RADYN, the Hα profile eventually returns

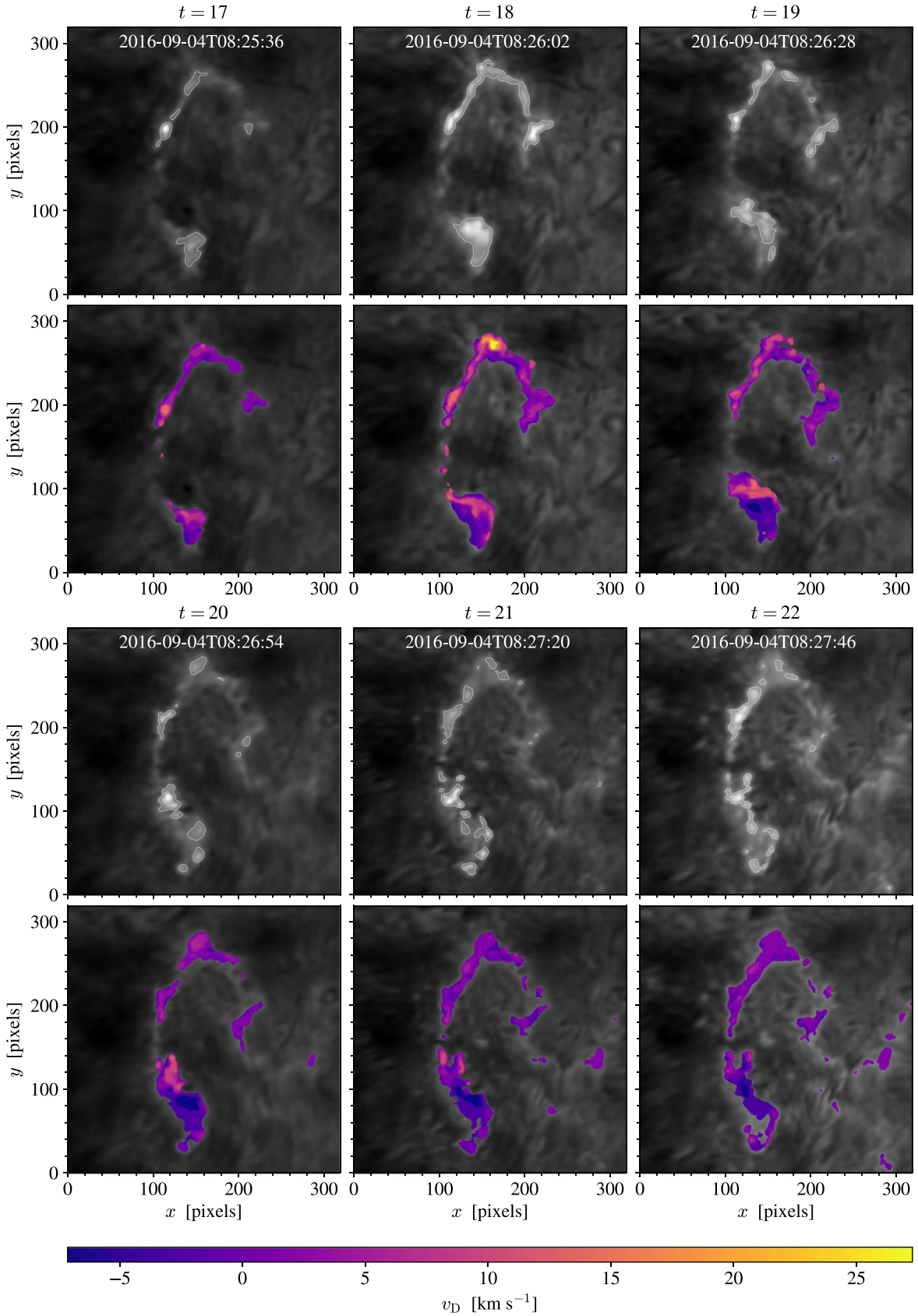

Figure 10. Intensity maps of the SST/CHROMIS Ca II K line core for six consecutive time steps during the flare. The contours in the top panels of each time step show the threshold (contours) used for the sampling of the *k*-means training data, for the analysis focused on the ribbon spectra. In the bottom panels of each time step, we overplot, on the intensity maps, the map of Doppler shift of the RSPs (clusters (1)–(32) shown in Figure 8). The f.o.v. has been reduced to mostly cover the ribbon.

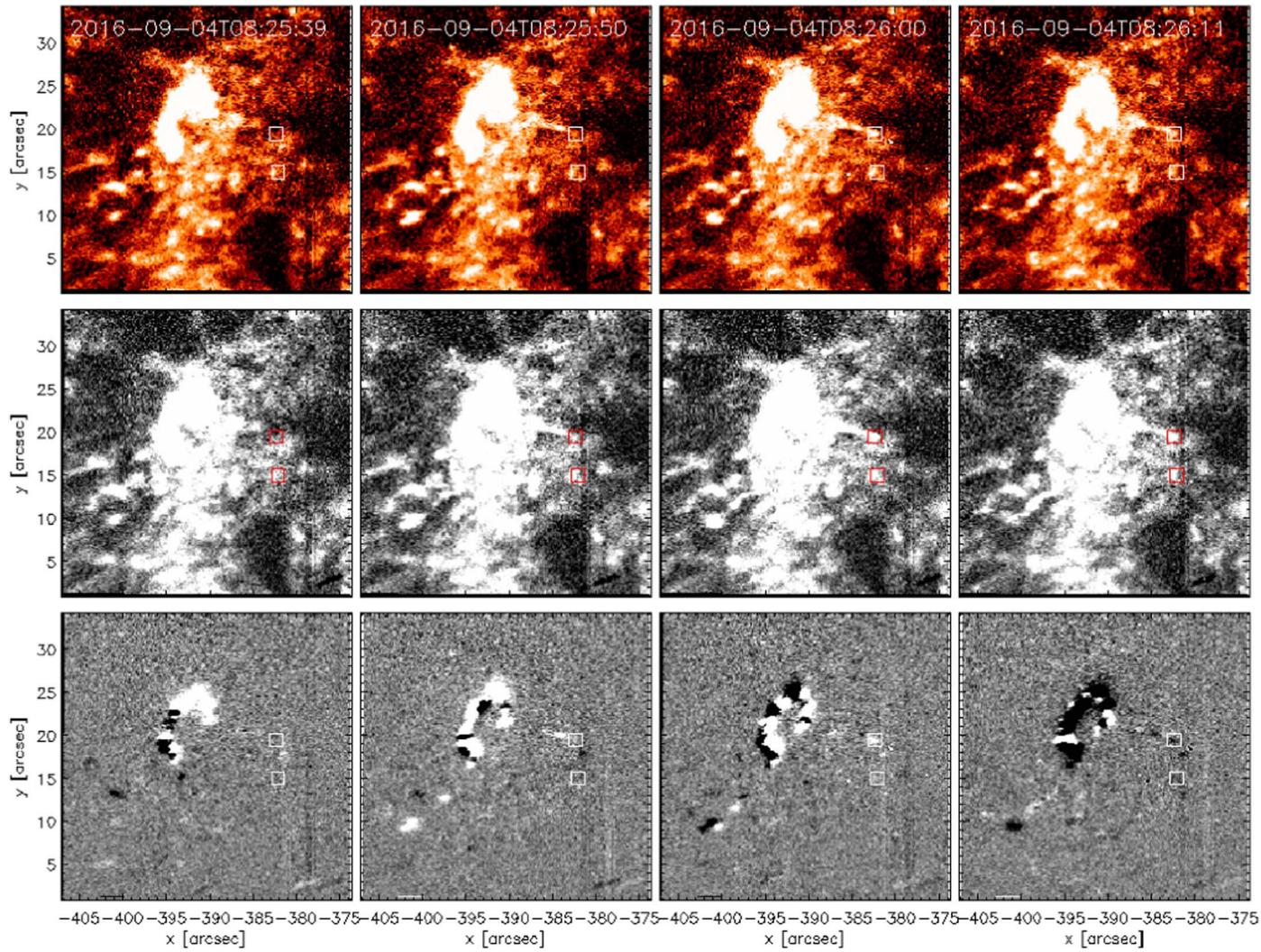

Figure 11. IRIS SJI time series around a time when part of the ribbon is under the IRIS slit. From top to bottom: IRIS 1400 Å SJI emission (top); base difference (i.e., the emission subtracted of the image at a reference time, which we chose to be 2016-09-04T08:19:35; middle); and running difference (i.e., the difference between the current SJI image and the SJI image from the immediately preceding time step; bottom). The two squares indicate the position for which we show the IRIS and CHROMIS Ca II spectra in Figure 12 (for better contrast, we use a red color for the boxes in the middle panels). The emission of the ribbon is quite weak at those locations, motivating the saturated color scales we used in the plots of this figure to highlight their emission as much as possible.

back to being in absorption during the post-heating phase (after 10 s). The heating mechanisms of the actual flare are more complicated, and after the peak of the flare, there is still ongoing heating that continuously changes the shape, width, and intensity of the profiles over time. However, at the northern (column (a)) and central (column (b)) locations of the ribbon, the profiles seem to slowly revert back into absorption, which is consistent with the simulation. The location in the southern region of the ribbon (column (c)) shows less variation of the Hα intensity and profile features after 8 minutes compared to the other locations.

The comparison of the IRIS spectral properties during the brightenings, with the expectations from RADYN models, can guide us in the interpretation of the observations and how they constrain the heating properties. As discussed at length in previous work (Testa et al. 2014; Polito et al. 2018; Testa et al. 2020), the grid of RADYN simulations of impulsively heated loops that we have carried out provide diagnostics of the presence of nonthermal particles and their properties. In particular, the blueshifts in the Si IV profiles, or Mg II triplet emission, are signatures of accelerated particles. The IRIS spectral properties of the earlier brightening are overall reminiscent of model H1 (which is a hybrid model, with half-length of 15 Mm, where half of the energy is transported by thermal conduction, and half goes into nonthermal particles) of Testa et al. (2020), in particular, the multicomponent nature of the Si IV profile with a blueshifted peak, the slightly higher blue peak in the Mg II profiles, and the lack of significant Mg II triplet emission. We can speculate that the IRIS profiles, and modest intensities of the brightenings, suggest that the heating is due to a mix of direct heating with thermal conduction and nonthermal particles, characterized by low energy (likely around 5 keV) and total energy and flux likely smaller than in our existing simulations. In fact, as we discussed in Polito et al. (2018), impulsive heating with nonthermal particles can produce Si IV blueshifts for lower-energy cutoff values when the total energy is reduced (their Figure 15). As discussed earlier in this section, such a model produces Hα profiles also similar to the observed ones. For the second brightening, the spectral profiles do not clearly point to the presence of nonthermal particles, but also for this case, some of the observed spectral properties are qualitatively similar to the

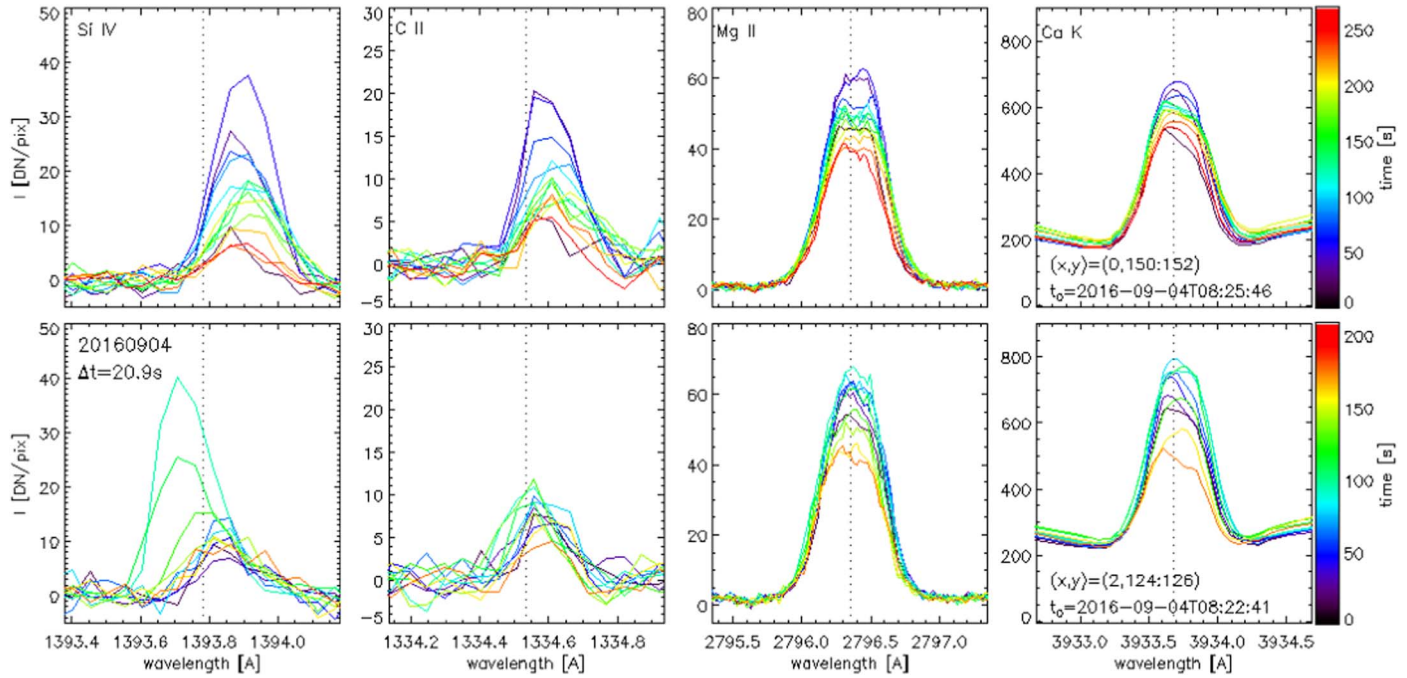

Figure 12. Temporal evolution of the spectral emission in IRIS TR and chromospheric lines and in the SST/CHROMIS Ca II K line (from left to right, Si IV 1393 Å, C II 1334 Å, Mg II 2796 Å, Ca II 3934 Å) for two locations (one in each row) where faint part of the ribbons is under the IRIS slit. For the CHROMIS Ca II spectra, we use 3933.684 Å as a reference wavelength (see Section 2 for details). The top and bottom rows correspond respectively to the northernmost and southernmost boxes of Figure 11. Note that the two time series have different timescales (see colorbars to the right) and start times (t_0 is noted in the right plot).

models with low-energy NTE ($E_C \sim 5$ keV), in particular in terms of the lack of significant Doppler shift in Si IV and of significant Mg II triplet emission (see also Figure 2 of Cho et al. 2023).

There are a few caveats to keep in mind when using the RADYN simulations of impulsively heated loops to interpret the observations we are analyzing here. First, these simulations do not reproduce the observed Mg II and Ca II (and often also the C II) profiles, particularly failing to reproduce the often observed single-peak profiles, as discussed above (and in previous works, such as, e.g., Testa et al. 2020). The mismatch between modeled and observed chromospheric profiles occurs also in quiescent plasma (e.g., Carlsson et al. 2015; Hansteen et al. 2023), and suggests that the background atmosphere might be a nonnegligible cause of the problem. Furthermore, these simulations, as described earlier in this section, were developed to match short-lived brightenings typically observed to last less than one minute, and therefore might not be an ideal comparison for the observations in this paper, which have longer duration (~2–4 minutes) footpoint brightenings. Also, the observations we analyzed have about 21 s cadence (and only ~0.5 s exposure time); therefore, the temporal sampling is such that it might have missed a crucial initial phase of the brightening(s), including possibly the peak of the emission.

4. Discussion and Conclusions

In this paper, we have analyzed coordinated imaging and spectroscopic observations of a small heating event in the core of an active region, observed with IRIS, SDO/AIA, and the CHROMIS instrument at SST. The atmospheric response to the heating includes the initial brightening at the footpoints of the coronal loops, visible in the chromospheric and TR emission in IRIS, SST, and AIA data, and the subsequent brightenings of the coronal loops, first in the hot AIA 131 Å (Fe XXI) emission, followed by the 94 Å (Fe XVIII) and other cooler channels during the cooling phase.

The morphology of the hot coronal loops, with sets of transient loops crossing at a significant angle, is reminiscent of what is generally observed in other similar heating events in AR cores (e.g., Testa et al. 2013, 2014; Reale et al. 2019a; Testa & Reale 2020; Testa et al. 2020), suggesting such events might be driven by large-scale photospheric motions or large-scale magnetic flux emergence (see also Asgari-Targhi et al. 2019). The coronal emission points to high temperatures up to ~10 MK, analogous to other small heating events in AR cores (see, e.g., Brosius et al. 2014; Ishikawa et al. 2017; Ishikawa & Krucker 2019; Reale et al. 2019a, 2019b; Testa & Reale 2020; Testa et al. 2020; Cooper et al. 2021). During the overall heating event, a first set of footpoint brightenings are observed (around 8:24UT) including one location under the IRIS slit (bottom row of Figure 12, and southernmost location marked in Figure 11) and the footpoints of a set of short loops (sampled by location (A) of Figure 3). The brightest chromospheric and TR brightenings are observed about 2 minutes later at the footpoints of a longer set of loops (sampled by location (B) of Figure 3), and are well observed by CHROMIS and the IRIS SJI (see, e.g., Figure 1), while only a weaker tail of this ribbon is observed under the IRIS slit (top row of Figure 12, and northernmost location marked in Figure 11).

The simultaneous IRIS and CHROMIS observations provide complementary diagnostics of the heating event. This CHROMIS data set is in particular characterized by exceptional spatial resolution down to ~100 km. The spatial analysis of the SST observations of the ribbon indicates spatial scales of ~150–200 km (measured FWHM ~0.″2–0.″3) for the chromospheric emission. There is a small observed spatial offset (~0.″2) between the SST chromospheric emission and the TR IRIS SJI emission in a direction compatible with the observed

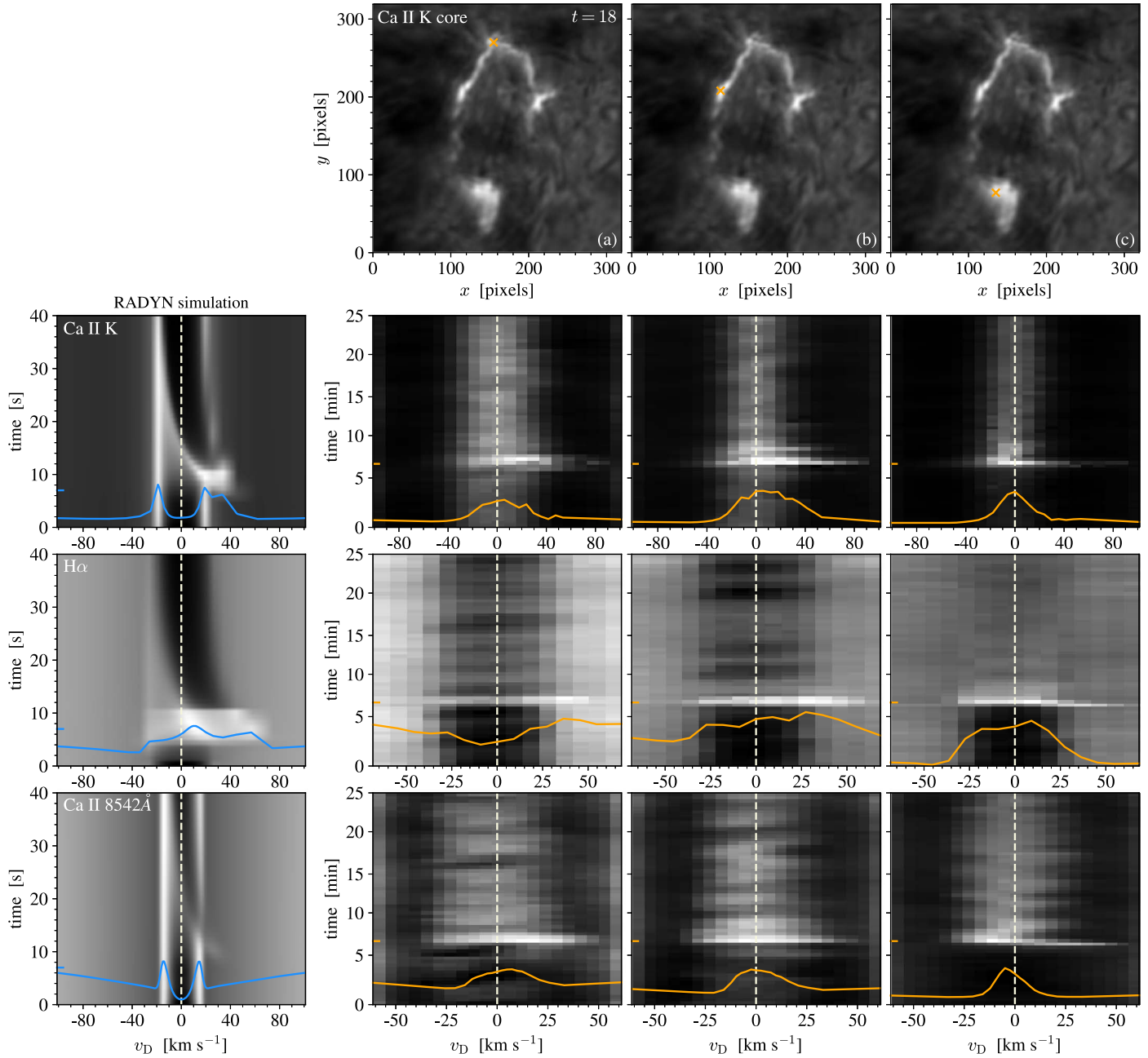

Figure 13. Spectral evolution of Ca II K, Hα, and Ca II 8542 Å in a RADYN simulation of a nanoflare-heated loop and from SST observations at different locations in the ribbon. The top panels show intensity maps of the SST/CHROMIS Ca II K line core at $t = 18$, where the ribbon locations at which the spectra are taken are marked as orange crosses. Each spectral evolution panel (the three bottom rows) shows the line profile at a time step during the flare phase. For the RADYN simulation, the time step is chosen at 7 s while the line profiles from the observations are chosen at 6.8 minutes (which is at $t = 18$). These time steps are marked along the y-axis. We note that the scaling of the x-axes varies between the observational data sets.

geometry, i.e., with the coronal loops extending in the east direction, and therefore the TR also extending to the east of the lower atmospheric emission observed by SST, although we cannot completely rule out small misalignment errors (see discussion in Section 3.2). The relative intensity of the TR (IRIS SJI 1400 Å) to lower chromospheric emission (observed with CHROMIS) is observed to vary over the ribbon, in particular with relatively weaker TR emission close to the two ends of the ribbon (i.e., south of $y \sim 45$, or west of $x \sim -390$, such as, e.g., location (C) of Figure 4), which suggests (see, e.g., Figure 5; and discussions in Testa et al. 2020) that in those locations the heating and energy transport mechanisms might less efficiently heat the TR, indicating for instance less direct heating and thermal conduction, and/or harder NTE, compared to other ribbon locations.

CHROMIS provides simultaneous spectral data in every spatial pixel, and therefore a trove of constraints for the spatial and temporal properties of the heating. In order to more efficiently exploit this information, we applied machine-learning methods to the CHROMIS Ca II K data, and in particular k-means clustering analyses, which can efficiently sort the observed spectra into groups with similar spectral properties (RSPs). This analysis reveals that the chromospheric emission is characterized by spatial and temporal coherence, in turn suggesting spatial and temporal coherence of the heating properties. In particular, in most ribbon locations, the Ca II

spectra rapidly evolves from initial narrower profiles with modest Doppler shift toward redshifted and broader profiles (see Figures 7 and 10), as the ribbon evolves and moves, mostly northward. This connection between the spectral evolution and ribbon motion puts tight constraints on models. The observed spectral evolution can likely be ascribed to either an evolution of the heating properties (e.g., harder nonthermal electron distributions in newly reconnected lines) and/or the evolution of the atmosphere as it gets denser and hotter, in response to the heating. A small fraction of Ca II spectra is blueshifted, and those blueshifted profiles are mostly concentrated in the southern region of the bright ribbon. The blueshifted profiles are generally narrower, and with lower intensities, than the redshifted profiles (see Figure 9). The very interesting correlations between Ca II Doppler shift, line width, and intensity provide valuable constraints for models. If the Doppler shifts of the Ca II spectral profiles are linked to plasma bulk velocities in the lower chromosphere, the correlations between the Doppler shift and line width could indicate a relationship between the plasma flows and the causes of line broadening (e.g., opacity broadening, superposition of plasma flows along the line of sight).

For a couple of low brightness ribbon locations, we obtained IRIS and CHROMIS spectra that could be used for a more constraining comparison with predictions from RADYN models of impulsively heated loops. For these locations, the Ca II K profiles are similar to what is observed in the low-intensity regions of the main ribbon, and in IRIS, no significant Mg II triplet emission is observed (which would have been a clear signature of high-energy nonthermal particles), and the Mg II spectra show mostly single-peaked profiles. The IRIS Si IV and C II emission shows slightly different properties in the two locations, with the earlier brightening showing blueshifted Si IV spectra and small C II enhancement, and the later brightening characterized by no significant Doppler shift change during the heating event and comparable increase of emission in Si IV and C II.

The comparison of these observed spectral properties with the prediction from models generally suggests the presence of low-energy nonthermal particles (with low-energy cutoff ∼5–10 keV), likely accompanying direct heating in the corona transported by thermal conduction. We note however that the grid of models we are using (Polito et al. 2018; Testa et al. 2020; Bakke et al. 2022) was developed to reproduce observed brightenings with shorter duration (<1 minutes) than the ones observed here. Also, as we discussed in detail in Section 3.5, the synthetic profiles from these models generally fail to reproduce some of the chromospheric line shapes, particularly the single-peaked profiles in C II, Mg II and Ca II, so we carried out only a qualitative comparison with the observations (e.g., in terms of Doppler shifts).

Magnetic reconnection is generally accepted to play a significant role in small heating events, especially in the core of active regions. The specific properties of these events, and, for instance, whether they behave like scaled-down versions of larger flares, are highly debated. In this context, the study of accelerated particles in these events can shed light into the nature of the heating mechanisms and of particle acceleration processes as well. Recent works have revealed the presence of accelerated particles in very small heating events, although typically these are characterized by a smaller low-energy cutoff and steeper slopes ($E_C \sim 5$–15 keV, $\delta \gtrsim 7$) compared with larger flares (e.g., Hannah et al. 2008; Testa et al. 2014; Wright et al. 2017; Glesener et al. 2020; Testa et al. 2020; Cooper et al. 2021; see also review of Testa & Reale 2023, and references therein). These findings were based on diagnostics from direct detection of nonthermal particle emission at hard X-ray wavelengths (e.g., with RHESSI, FOXSI, NuSTAR; Lin et al. 2002; Harrison et al. 2013; Glesener et al. 2016), or spectral diagnostics from the indirect detection of the effect of nonthermal particles in the lower atmosphere where they can deposit most of their energy (e.g., with IRIS, and with ground-based data such as the SST data analyzed here). Recent work by Polito et al. (2023) presented rare simultaneous observations with IRIS and NuSTAR, which provided independent diagnostics of nonthermal particles and found concordant results from both approaches. Also in this latter case, the nonthermal particle distribution was characterized by relatively low energies ($E_C \sim 8$ keV) and steep slopes, analogous to the properties of the heating event we studied here, as inferred from the comparison of IRIS and SST spectra with RADYN simulations.

The observations analyzed here put tight constraints on the models, but also highlight the shortcomings of the models. In fact, although they provide a good match for the observed TR Si IV profiles (and occasionally reproduce some chromospheric spectral profiles, such as the Hα case discussed in Section 3.5), they generally fail at producing chromospheric spectral line shapes similar to the observations as also discussed in previous work (e.g., Polito et al. 2018; Testa et al. 2020; Cho et al. 2023). We note that these discrepancies between models and observed profiles occur also in quiescent atmosphere (see, e.g., Hansteen et al. 2023, and references therein). A necessary next step is therefore to investigate in detail the cause of these discrepancies and improve the model to remediate them, and allow us to fully exploit these diagnostics.

Acknowledgments

We thank the referee for a careful review of the paper and several suggestions that have helped improve the paper. We thank Vanessa Polito for the use of previously published RADYN simulations. P.T. is funded for this work by contracts 8100002705 (IRIS), and NASA contract NNM07AB07C (*Hinode*/XRT) to the Smithsonian Astrophysical Observatory, and by NASA grant 80NSSC20K1272. B.D.P. is supported by NASA contract NNG09FA40C (IRIS). This research has made use of NASA's Astrophysics Data System and of the SolarSoft package for IDL. SDO data were obtained courtesy of NASA/SDO and the AIA and HMI science teams. IRIS is a NASA small explorer mission developed and operated by LMSAL with mission operations executed at NASA Ames Research Center and major contributions to downlink communications funded by ESA and the Norwegian Space Centre. The Swedish 1 m Solar Telescope is operated on the island of La Palma by the Institute for Solar Physics of Stockholm University in the Spanish Observatorio del Roque de los Muchachos of the Instituto de Astrofísica de Canarias. The Institute for Solar Physics is supported by a grant for research infrastructures of national importance from the Swedish Research Council (registration number 2021-00169). This research is supported by the Research Council of Norway, project numbers 250810, 325491, and through its Centres of Excellence scheme, project number 262622.

ORCID iDs

Paola Testa https://orcid.org/0000-0002-0405-0668
Helle Bakke https://orcid.org/0000-0002-2503-3269
Luc Rouppe van der Voort https://orcid.org/0000-0003-2088-028X
Bart De Pontieu https://orcid.org/0000-0002-8370-952X

References

Allred, J., Kowalski, A., & Carlsson, M. 2015, AAS/AGU Triennial Earth-Sun Summit, 1, 302.07
Antiochos, S. K., Karpen, J. T., DeLuca, E. E., Golub, L., & Hamilton, P. 2003, ApJ, 590, 547
Arthur, D., & Vassilvitskii, S. 2007, k-means++: the advantages of careful seeding in SODA '07: Proc. of the Eighteenth Annual ACM-SIAM Symp. on Discrete Algorithms (New York: ACM), 1027
Asgari-Targhi, M., van Ballegooijen, A. A., & Davey, A. R. 2019, ApJ, 881, 107
Bakke, H., Carlsson, M., Rouppe van der Voort, L., et al. 2022, A&A, 659, A186
Berger, T. E., De Pontieu, B., Schrijver, C. J., & Title, A. M. 1999, ApJL, 519, L97
Boerner, P., Edwards, C., Lemen, J., et al. 2012, SoPh, 275, 41
Boerner, P. F., Testa, P., Warren, H., Weber, M. A., & Schrijver, C. J. 2014, SoPh, 289, 2377
Bose, S., Henriques, V. M. J., Joshi, J., & Rouppe van der Voort, L. 2019, A&A, 631, L5
Brooks, D. H., Warren, H. P., Williams, D. R., & Watanabe, T. 2009, ApJ, 705, 1522
Brosius, J. W., Daw, A. N., & Rabin, D. M. 2014, ApJ, 790, 112
Carlsson, M., Leenaarts, J., & De Pontieu, B. 2015, ApJL, 809, L30
Carlsson, M., & Stein, R. F. 1992, ApJL, 397, L59
Carlsson, M., & Stein, R. F. 1995, ApJL, 440, L29
Carlsson, M., & Stein, R. F. 1997, ApJ, 481, 500
Cho, K., Testa, P., De Pontieu, B., & Polito, V. 2023, ApJ, 945, 143
Cooper, K., Hannah, I. G., Grefenstette, B. W., et al. 2021, MNRAS, 507, 3936
de la Cruz Rodríguez, J., Löfdahl, M. G., Sütterlin, P., Hillberg, T., & Rouppe van der Voort, L. 2015, A&A, 573, A40
De Pontieu, B., Title, A. M., Lemen, J. R., et al. 2014, SoPh, 289, 2733
Fletcher, L., & De Pontieu, B. 1999, ApJL, 520, L135
Glesener, L., Krucker, S., Christe, S., et al. 2016, Proc. SPIE, 9905, 99050E
Glesener, L., Krucker, S., Duncan, J., et al. 2020, ApJL, 891, L34
Hannah, I. G., Christe, S., Krucker, S., et al. 2008, ApJ, 677, 704
Hansteen, V. H., Martinez-Sykora, J., Carlsson, M., et al. 2023, ApJ, 944, 131
Harrison, F. A., Craig, W. W., Christensen, F. E., et al. 2013, ApJ, 770, 103
Ishikawa, S.-n., Glesener, L., Krucker, S., et al. 2017, NatAs, 1, 771
Ishikawa, S.-n., & Krucker, S. 2019, ApJ, 876, 111
Klimchuk, J. A. 2006, SoPh, 234, 41
Klimchuk, J. A. 2015, RSPTA, 373, 20140256
Kobayashi, K., Cirtain, J., Winebarger, A. R., et al. 2014, SoPh, 289, 4393
Lemen, J. R., Title, A. M., Akin, D. J., et al. 2012, SoPh, 275, 17
Lin, R. P., Dennis, B. R., Hurford, G. J., et al. 2002, SoPh, 210, 3
Löfdahl, M. G., Hillberg, T., de la Cruz Rodríguez, J., et al. 2021, A&A, 653, A68
MacQueen, J. 1967, in Proc. Fifth Berkeley Symp. on Mathematical Statistics and Probability, 1, ed. L. M. Le Cam & J. Neyman (Berkeley, CA: Univ. California Press), 281
Martens, P. C. H., Kankelborg, C. C., & Berger, T. E. 2000, ApJ, 537, 471
Neckel, H. 1999, SoPh, 184, 421
Panos, B., Kleint, L., Huwyler, C., et al. 2018, ApJ, 861, 62
Pereira, T. M. D., & Uitenbroek, H. 2015, A&A, 574, A3
Peres, G., Reale, F., & Golub, L. 1994, ApJ, 422, 412
Pesnell, W. D., Thompson, B. J., & Chamberlin, P. C. 2012, SoPh, 275, 3
Polito, V., Peterson, M., Glesener, L., et al. 2023, FrASS, in press
Polito, V., Testa, P., Allred, J., et al. 2018, ApJ, 856, 178
Reale, F. 2014, LRSP, 11, 4
Reale, F., Testa, P., Petralia, A., & Graham, D. R. 2019a, ApJ, 882, 7
Reale, F., Testa, P., Petralia, A., & Kolotkov, D. Y. 2019b, ApJ, 884, 131
Rouppe van der Voort, L., De Pontieu, B., Scharmer, G. B., et al. 2017, ApJL, 851, L6
Rouppe van der Voort, L. H. M., De Pontieu, B., Carlsson, M., et al. 2020, A&A, 641, A146
Scharmer, G. 2017, SOLARNET IV: The Physics of the Sun from the Interior to the Outer Atmosphere, 85
Scharmer, G. B., Bjelksjo, K., Korhonen, T. K., Lindberg, B., & Petterson, B. 2003a, Proc. SPIE, 4853, 341
Scharmer, G. B., Dettori, P. M., Lofdahl, M. G., & Shand, M. 2003b, Proc. SPIE, 4853, 370
Scharmer, G. B., Narayan, G., Hillberg, T., et al. 2008, ApJL, 689, L69
Testa, P., De Pontieu, B., Allred, J., et al. 2014, Sci, 346, B315
Testa, P., De Pontieu, B., Martínez-Sykora, J., et al. 2013, ApJL, 770, L1
Testa, P., Polito, V., & Pontieu, B. D. 2020, ApJ, 889, 124
Testa, P., & Reale, F. 2020, ApJ, 902, 31
Testa, P., & Reale, F. 2023, in Handbook of X-ray and Gamma-ray Astrophysics, ed. C. Bambi & A. Santangelo (Berlin: Springer), 134
Tripathi, D., Mason, H. E., Del Zanna, G., & Young, P. R. 2010, A&A, 518, A42
Uitenbroek, H. 2001, ApJ, 557, 389
van Noort, M., Rouppe van der Voort, L., & Löfdahl, M. G. 2005, SoPh, 228, 191
Vissers, G. J. M., de la Cruz Rodríguez, J., Libbrecht, T., et al. 2019, A&A, 627, A101
Wright, P. J., Hannah, I. G., Grefenstette, B. W., et al. 2017, ApJ, 844, 132